Thermal and electrochemical properties of PEO-LiTFSI-Pyr$_{14}$ TFSI-based composite cathodes, incorporating 4 V-class cathode active materials

Morten Wetjen [a], Guk-Tae Kim [a,*], Mario Joost [a], Giovanni B. Appetecchi [b], Martin Winter [a], Stefano Passerini [a,**]

[a] University of Muenster, Institute of Physical Chemistry, MEET Battery Research Center, Corrensstr. 46, 48149 Muenster, Germany
[b] ENEA, Agency for New Technologies, Energy and Sustainable Economic Development, UTRINN-IFC, Via Anguillarese 301, Rome 00123, Italy

HIGHLIGHTS

- 4 V-class composite cathodes show excellent mechanical properties and high thermal stabilities.
- Li/SPE/Li(Ni$_{0.8}$Co$_{0.15}$Al$_{0.05}$)O$_2$ batteries indicate high discharge capacities.
- Pyr14TFSI ionic liquid improves the interfacial properties of the composite cathode.
- The anodic cut-off potential greatly influences the battery impedance evolution.
- No continuous decomposition of PEO could be observed in presence of the 4 V-class cathode active material.

ARTICLE INFO

ABSTRACT

Poly(ethylene oxide)-lithium bis(trifluoromethanesulfonyl)imide *N*-butyl-*N*-methylpyrrolidinium bis(-trifluoromethanesulfonyl)imide (PEO-LiTFSI-Pyr$_{14}$TFSI)-based 4 V-class composite cathodes, incorporating either Li(Ni$_{1/3}$Co$_{1/3}$Mn$_{1/3}$)O$_2$ or Li(Ni$_{0.8}$Co$_{0.15}$Al$_{0.05}$)O$_2$ were prepared by a hot-pressing process and successively investigated in terms of their morphological, thermal, and electrochemical properties. Thereby, excellent mechanical and thermal properties could be demonstrated for all composite cathodes. The electrochemical performance of truly dry all-solid-state Li/P(EO)$_{10}$LiTFSI-(Pyr$_{14}$TFSI)$_2$/composite cathode batteries at temperatures as low as 40 °C revealed high delivered capacities. However, in comparison with LiFePO$_4$, the 4 V-class composite cathodes also indicated much lower capacity retention. In-depth investigations on the interfacial properties of Li(Ni$_{0.8}$Co$_{0.15}$Al$_{0.05}$)O$_2$ composite cathodes revealed a strong dependence on the anodic cut-off potential and the presence of current flow through the cell, whereby different degradation mechanisms could be characterized upon cycling, according to which the finite growth of a surface films at both electrode/polymer electrolyte interfaces inhibited continuous decomposition of the polymer electrolyte even at potentials as high as 4.3 V. Moreover, the presence of Pyr$_{14}$TFSI in the 4 V-class composite cathodes sustainably reduced the cathode interfacial resistance and presumably diminished the corrosion of the aluminum current collector.

1. Introduction

During the last two decades, Li-ion batteries have revolutionized the portable consumer electronics market due to their light and compact design, combined with a working voltage of about 4 V and a high specific energy [1]. However, in terms of future challenges arising from the electrification of transportation and large-scale stationary energy storage of intermittent renewable energy sources, Li-ion technology suffers a drawback from severe safety issues, emerging from the volatile and flammable nature of liquid alkyl-carbonate-based electrolytes that are typically used in Li-ion batteries [2].

All-solid-state lithium metal polymer batteries in which the anode, electrolyte and cathode are flexible thin films not only facilitate the assembly and versatility in battery shape/design, but also enable significant improvements in terms of safety and performance [3]. As a result of the low atomic weight and highly

* Corresponding author. Tel.: +49(0)251 83 23425; fax: +49(0)251 83 36032.
** Corresponding author. Tel.: +49(0)251 83 36026; fax: +49(0)251 83 36032.
E-mail addresses: kimguktae@uni-muenster.de (G.-T. Kim), stefano.passerini@uni-muenster.de (S. Passerini).

electropositive potential of lithium metal, lithium metal polymer batteries offer high cell potentials and high energy densities, which are mainly limited by the cathode active material [4,5].

Since their proposal by Armand et al., solid polymer electrolytes (SPEs) were extensively studied, whereby poly(ethylene oxide)-based systems emerged as the most promising candidate [6]. The recent development by Bollore' of pure electric vehicles (Blue car) using lithium metal polymer batteries based poly(ethyleneoxide) − LiX as electrolyte is renewing the interest in the field. These batteries operates at moderate temperatures (60−90 °C), however, ternary solid polymer electrolytes, comprising poly(ethylene oxide) (PEO), lithium bis(trifluoromethanesulfonyl)imide (LiTFSI) salt, and N-butyl-N-methylpyrrolidinium bis(trifluoromethanesulfonyl) imide (Pyr$_{14}$TFSI) ionic liquid showed good interfacial stability toward lithium metal, good mechanical properties, and reasonable ionic conductivity even at lower temperatures [7−9].

The utilization of solid polymer electrolytes and consequently the absence of liquid solution require careful engineering of the cathode electrode. Hence, typical composite cathode electrodes for lithium metal polymer batteries consist of an electrode fraction, including the cathode active material and electronically conductive carbon, and an ionically conductive polymer electrolyte fraction, comprising a high-molecular weight PEO-based polymer and a lithium salt (e.g. LiTFSI, LiBF$_4$) [10,11]. As a consequence of the poor oxidative resistivity of the ethylene oxide segments of PEO-based polymer electrolytes and their corresponding low thermodynamic stability at highly electronegative potentials (>4 V vs. Li/Li$^+$), lithium metal polymer battery researchers were first exclusively focused on moderate 3 V-class cathode active materials, inter alia LiFePO$_4$ and V$_2$O$_5$ [12,13]. However, highly electronegative 4 V-class cathode active materials offer high cell potentials and high energy, when combined with lithium metal anode electrodes, so that during the last decade various strategies were pursued to enable the utilization of high potential cathode active materials in all-solid-state lithium metal polymer batteries. Among them, Kobayashi et al. proposed a composite concept, in which a 4 V-class cathode active material (e.g. LiMn$_2$O$_4$, LiCoO$_2$) was either coated or mixed with a highly oxidation resistive ceramic electrolyte, such as (Li,La)TiO$_3$ or Li$_3$PO$_4$, thus forming a protective film at the solid polymer electrolyte/cathode [14−16]. In contrast, Takeda et al. investigated a hyper-branched polymer-plasticized, PEO-LiTFSI-LiPF$_6$-BaTiO$_3$ solid polymer electrolyte with 4 V-class Li(Ni$_{0.8}$Co$_{0.2}$) O$_2$ composite cathodes [17,18], while Sakai and co-workers reported plasticized high-MW(10^5−10^6) comb-shaped, polyether-based LiCoO$_2$ composite cathodes [11,19]. Nevertheless, no 4 V-class all-solid-state lithium metal polymer battery, was reported to date, which could compete with LiFePO$_4$-based composite cathodes in terms of delivered capacity and cyclability, respectively, at operating temperatures as low as 40 °C.

Inspired by the excellent electrochemical performance of cross-linked PEO-LiTFSI-Pyr$_{14}$TFSI ternary solid polymer electrolytes, showing an anodic stability exceeding 4.5 V vs. Li/Li$^+$ at 40 °C and outstanding battery performance of derivative LiFePO$_4$ composite cathodes, the present work focused on the establishment of 4 V-class cathode active materials in PEO-LiTFSI-Pyr$_{14}$TFSI-based composite cathodes [20,21]. The incorporation of Pyr$_{1A}$TFSI ionic liquids into PEO-LiTFSI-based composite cathode was reported to have beneficial impact on the resulting reversible capacity and rate capability, in particular at near ambient temperatures [22−24]. Moreover, the ionic liquid considered here owns further advantageous properties, including negligible volatility, non-flammability, high thermal stability, and high ionic conductivity [25−27], thus making it quite suitable for electrochemical applications.

Now, the PEO-LiTFSI-Pyr$_{14}$TFSI-based approach is transferred to high potential composite cathodes. To the best of our knowledge, this is the first report about a 4 V-class composite cathode comprising an ionic liquid. Hence, Li(Ni$_{0.8}$Co$_{0.15}$Al$_{0.05}$)O$_2$ (NCA) and Li(Ni$_{1/3}$Co$_{1/3}$Mn$_{1/3}$)O$_2$ (NCM), which are already well established in Li-ion batteries, are the cathode active materials of choice, due to their high potential (in average 3.8 V vs. Li/Li$^+$) and high specific capacity (190 mAh g^{-1} and 160 mAh g^{-1}, respectively) when charged up to 4.3 V [28,29].

The 4 V-class composite cathodes were investigated in terms of their mechanical as well as morphological properties through scanning electron microscopy. The thermal stability was evaluated by thermogravimetric analysis and differential scanning calorimetry, respectively. Galvanostatic cycling measurements of Li/SPE/ cathode lithium metal polymer batteries were combined with impedance spectroscopy to analyze the electrochemical behavior of the cell compounds as well as of their interfacial properties.

2. Experimental

2.1. Synthesis of the ionic liquid

The N-butyl-N-methylpyrrolidinium bis(trifluoromethanesulfonyl)imide (Pyr$_{14}$TFSI) ionic liquid was synthesized through a procedure described in detail elsewhere [30,31].

2.2. Preparation of cross-linked ternary solid polymer electrolyte

Cross-linked ternary solid polymer electrolyte (SPE) films were prepared through a solvent-free, hot-pressing process [3,20], that was performed in a very low relative humidity dry room (relative humidity $< 0.1\%$ at 20 °C). First, LiTFSI (*3M*) and Pyr$_{14}$TFSI were dried under turbo molecular vacuum (10^{-7} mbar) at 120 °C for at least 36 h, whereas PEO (*Dow Chemical*, WSR 301, molecular weight = 4,000,000) was dried under vacuum at 50 °C for 48 h. Benzophenone (*Aldrich*), which was used as photo-initiator for the cross-linking process, was directly dissolved in Pyr$_{14}$TFSI at 20 °C for 12 h. Thereby, the Bp/PEO weight ratio was fixed to 0.05, while the P(EO)/Li and (Pyr$_{14}$)$^+$/Li$^+$ mole ratio were set equal to 10 and 2, respectively, resulting in a PEO-LiTFSI-Pyr$_{14}$TFSI molar composition of 10/1/2, which in the following is also described as P(EO)$_{10}$LiTFSI-(Pyr$_{14}$TFSI)$_2$.

PEO and LiTFSI were intimately mixed in a glass vial and then added to the Bp/Pyr$_{14}$TFSI solution. Previous work has shown that this ratio represents a trade-off between high ionic conductivity and good lithium metal interfacial stability [7,9]. The so-obtained ternary PEO-LiTFSI-Pyr14TFSI blend was housed in a vacuum-sealed, pouch bag and successively annealed under vacuum at 100 °C overnight to produce a homogeneous rubber-like bulk material. The latter was sandwiched between two *Mylar* foils and hot-pressed at 100 °C for several minutes to manufacture 80 μm thick films. Finally, the ternary solid polymer electrolyte film was cross-linked using a UV Cube photo-irradiator (350 W Hg lamp) for 10 min [20,32]. All steps were performed in a dry room (relative humidity $< 0.1\%$ at 20 °C).

2.3. Preparation of the composite cathodes

The composite cathode tapes were prepared in a similar manner as the previous ternary solid polymer electrolyte films. Initially, active material (LiFePO$_4$ (LFP), *Süd Chemie*, Li(Ni$_{1/3}$Co$_{1/3}$Mn$_{1/3}$)O$_2$ (NCM) or Li(Ni$_{0.8}$Co$_{0.15}$Al$_{0.05}$)O$_2$ (NCA), both from *Toda*, each 43 wt %) and conductive carbon (Ketjenblack EC-300J, *Akzo Nobel*, 7 wt%), which were dried under vacuum at 120 °C for at least 24 h, were intimately mixed in a mortar. According to Fig. 1 (Panel A), a paste-like mixture of PEO (17.5 wt%), LiTFSI (5 wt%), and Pyr$_{14}$TFSI (27.5 wt%) was added to form a composite cathode blend. The
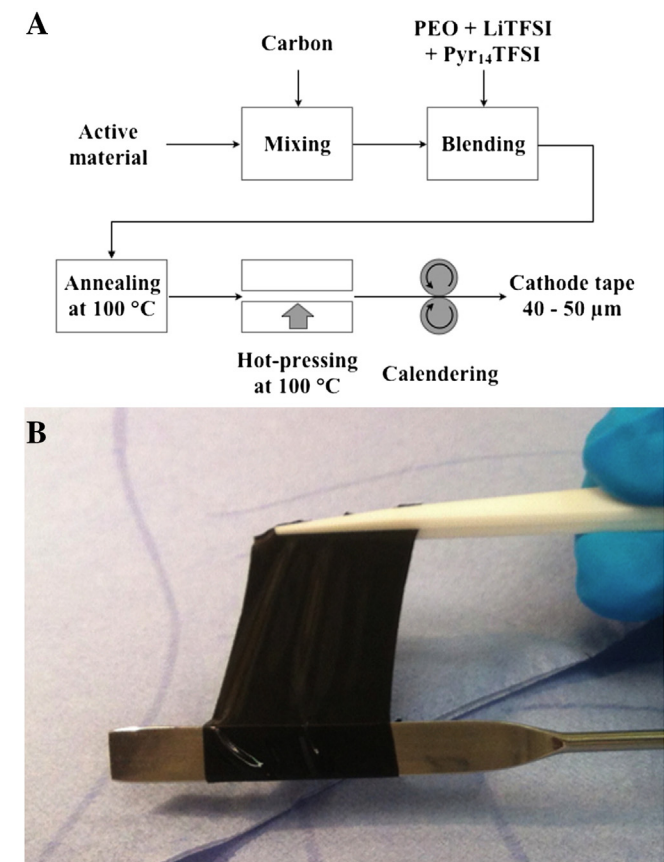
A

B

Fig. 1. Schematic illustration of the preparation of PEO-LiTFSI-Pyr$_{14}$TFSI-based composite cathode tapes (Panel A), and an image of a final composite cathode tape, comprising Li(Ni$_{1/3}$Co$_{1/3}$Mn$_{1/3}$)O$_2$ (NCM) as active material (Panel B).

resulting bulk material was annealed at 100 °C overnight and subsequently hot-pressed at 100 °C for several minutes to form a preliminary composite cathode tape of approximately 100 μm thickness. To obtain the final cathode, the tape was cold-calendered (final thickness 40–50 μm). For battery cell assembly, discs of 12 mm in diameter (electrochemical active area equal to 1.13 cm^2) were punched out of the composite cathode tape. The resulting active material mass loading ranged from 3 to 4 mg cm^{-2} for LFP and 4–5 mg cm^{-2} for NCM and NCA, respectively.

2.4. Composite cathode characterization

The manufactured composite cathodes were investigated in terms of their thermal properties using thermogravimetric analysis (TGA) and differential scanning calorimetry (DSC).

For TGA measurements, the composite cathode samples were hermetically sealed in aluminum pans, using a mass loading of about 5 mg. Prior to measurement the pans were automatically opened by the instrument. The procedure started with an isotherm step at 30 °C, meanwhile the chamber was purged with pure nitrogen gas for 30 min to remove any traces of oxygen. Finally, the temperature was continuously increased up to 600 °C, using a heating rate of 5 °C min^{-1}, while recording the weight change as a function of the temperature. The measurements were repeated on different samples using nitrogen atmosphere or oxygen atmosphere, whereas the gas flow rate was always adjusted to 25 mL min^{-1} [33].

For DSC measurements, the composite cathodes were hermetically sealed in aluminum pans, using a mass loading of about 7 mg. The procedure started with a cooling ramp from room temperature

to −140 °C, using a fast cooling rate of 10 °C min^{-1} to avoid crystallization. Afterwards the temperature was cycled between −100 °C and 150 °C, with a cooling rate of 10 °C min^{-1} and a heating rate of 5 °C min^{-1} [33].

The whole sample preparation was carried out in a dry room (relative humidity < 0.1% at 20 °C). The measurements were performed on a *TA thermogravimetric analyzer* (Model Q5000) and a *TA Instruments differential calorimeter* (Q2000), respectively.

Scanning electron microscopy (SEM) was used to investigate the morphology and the composition of the composite cathode tapes. A Bal-Tec sputter coater was employed to sputter the samples with gold for 30 s at 45 mA. The resulting thin film of gold atoms enhanced the electronic conductivity of the sample, in particular, of the polymer electrolyte fraction. Thus, local charge effects and melting of the PEO due to the high energy of the focused electron beam were reduced. The measurements were performed using an *Auriga Modular Crossbeam from Carl Zeiss*.

2.5. Test cell assembly

The electrochemical measurements on the composite cathodes were performed using vacuum-sealed, laminated two-electrode, symmetrical pouch cells fabricated inside the dry room. Two different kinds of cells were assembled either by sandwiching a cross-linked PEO-LiTFSI-Pyr$_{14}$TFSI ternary solid polymer electrolyte (SPE) film between two lithium metal electrodes Li/SPE/Li or by placing a SPE film between two composite cathode tapes, which in turn where sandwiched by aluminum foil current collectors Al^0/cathode/SPE/cathode/Al^0.

All-solid state Li/SPE/cathode lithium metal polymer battery cells (cathode limited) were fabricated by piling up a lithium foil (*Chemetall*, 50 μm thickness), a cross-linked ternary solid polymer electrolyte film and a composite cathode tape. Ni^0 foil and Al^0 foil were used as current collectors, respectively. The electrochemical active area was about 1.13 cm^2.

All cells for the anode and the cathode were assembled in the dry room, housed in vacuum-sealed (10^{-2} mbar) pouch bags, and successively laminated by hot-rolling at 100 °C.

2.6. Electrochemical tests

The cycling performance of the Li/SPE/cathode lithium metal polymer batteries, comprising either LiFePO$_4$ (LFP), Li(Ni$_{1/3}$Co$_{1/3}$Mn$_{1/3}$)O$_2$ (NCM) or Li(Ni$_{0.8}$Co$_{0.15}$Al$_{0.05}$)O$_2$ (NCA) cathode active material was investigated using a different galvanostatic charge/discharge procedures. First, the lithium metal polymer batteries were cycled at a constant rate of C/10 (C/20 in the first cycle), whereby the cut-off potentials were set to 4.0 V (charge) and 2.0 V (discharge) for LFP, as well as 4.3 V (charge) and 3.0 V (discharge) for NCM and NCA, in order to allow full capacity utilization and to investigate the capacity retention upon cycling. Second, the dependence of the anodic cut-off potential on the delivered capacity and cyclability of the 4 V-class composite cathodes was evaluated by cycling Li/SPE/NCA lithium metal polymer batteries to different anodic (charge) cut-off potentials between 4.0 V and 4.45 V, while the cathodic (discharge) cut-off potential was fixed to 3.0 V and the rate set to C/15 (∼0.06 mA cm^{-2}). All measurements were performed in a climatic chamber (*Binder* GmbH MK53) at 40 (±0.1) °C, using a Maccor S4000 battery tester as galvanostat.

AC impedance spectroscopy measurements were performed on symmetrical Li/SPE/Li and Al^0/cathode/SPE/cathode/Al^0 cells and asymmetrical Li/SPE/NCA lithium metal polymer batteries (65 kHz–100 mHz, 10 mV potential perturbation), using a *Frequency Response Analyzer* (Solartron model 1260), at times complemented by a *Electrochemical Interface* (Solartron model 1287), in

order to sustain and adjust cell potentials while measuring polarized and asymmetrical cells. During the measurements the cells were located in a climatic chamber at 20 °C (*Binder* GmbH MK53) with a temperature control of ±0.1 °C. The impedance responses were analyzed with ZView fit software (*Scribner Associates Inc.*), using a suitable equivalent circuit model.

3. Results and discussion

3.1. Mechanical properties

The mechanical properties and the morphology of both 4 V-class composite cathode were quite similar. As a consequence, in the following the results are exemplarily discussed by always one representative, i.e. either $Li(Ni_{1/3}Co_{1/3}Mn_{1/3})O_2$ (NCM) or $Li(Ni_{0.8}Co_{0.15}Al_{0.05})O_2$ (NCA).

Fig. 1 (Panel B) shows an image of the NMC composite cathode stretched between a spatula and a tweezers. As it can be seen, the thin tape of approximately 40 µm thickness demonstrated excellent mechanical stability and flexibility. Further processing and cutting of the cathode tape was handled with ease, thereby, the composite cathode tape did not stick to the scissor, ensuring sharp edges. Similar to previously reported cross-linked ternary solid polymer electrolytes, the composite cathode tape also exhibited some elasticity, albeit the degree of limiting elongation was much smaller compared to that of cross-linked ternary SPEs [20].

3.2. Morphology of the composite cathodes

To investigate the morphology of the PEO-LiTFSI-Pyr$_{14}$TFSI-based 4 V-class composite cathode tapes, scanning electron microscopy (SEM) measurements were performed. Fig. 2 (Panel A) shows a top-view of the composite cathode tape incorporating NCA as cathode active material. Accordingly, numerous NCA particles are dispersed throughout the polymer electrolyte fraction, consisting of PEO, LiTFSI, and Pyr$_{14}$TFSI. Hereby, the polymer electrolyte fraction acts like a continuous extension of the solid polymer electrolyte (SPE), thus facilitating the diffusion of lithium ions from the lithium anode to the active material in the composite cathode. As a consequence, the composition of the latter displays a trade-off between the active material-carbon weight fraction (43 wt% NCA, 7 wt% carbon) and the polymer electrolyte weight fraction (PEO 17.5 wt%, LiTFSI 5 wt%, Pyr$_{14}$TFSI 27.5 wt%). Indeed, a higher amount of the active material-carbon weight fraction results in an enhanced energy density per mass unit electrode, but also faces a closer and partially interrupted polymer matrix network, thus resulting in a limited availability and transport of lithium ions. Fig. 2 (Panel A), however, indicates that in the present composite cathode tape the NCA particles are well separated by a continuous polymer electrolyte fraction, which enables a steady lithium ion transport to the NCA particles. This observation is additionally confirmed by the cross-section view in Fig. 2 (Panel B), indicating that the NCA particles are not only dispersed at the composite cathode surface, but are also individually embedded within and throughout the cathode bulk.

The enlargement in Fig. 2 (Panel A) shows a magnification of an NCA particle, which is not only fully embedded into the polymer electrolyte fraction, but is also covered with polymer electrolyte. In terms of the charge-transfer between the polymer fraction and the active material particle, this observation is crucial, because a good physical contact is necessary to obtain a low interfacial resistance and thus a good electrochemical performance. In contrast, it can also be seen that the NCA particles within the cathode bulk are larger compared to those at the surface, which may be explained with a force gradient during cold-calendaring. Accordingly, the
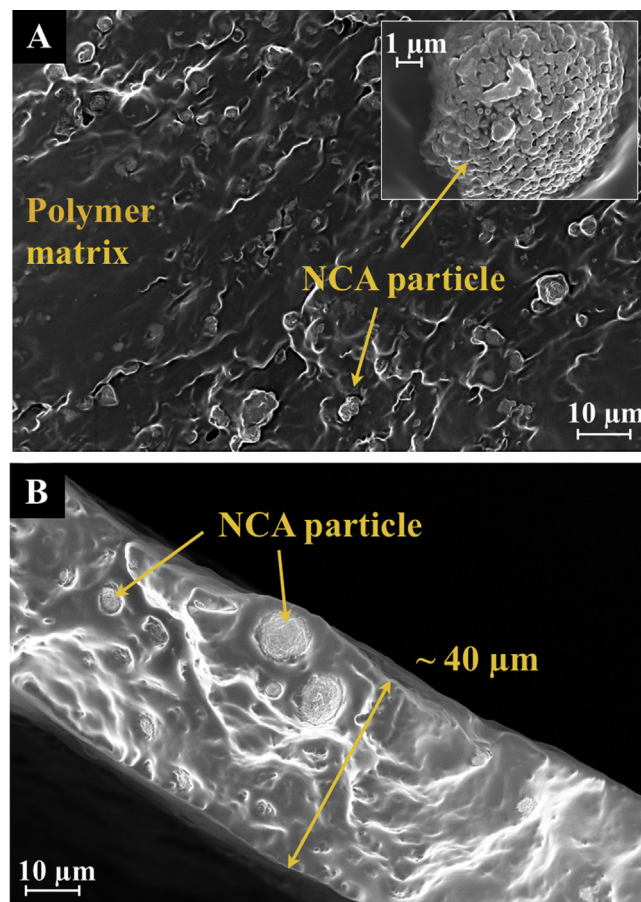

Fig. 2. Scanning electron microscopy (SEM) images of a PEO-LiTFSI-Pyr$_{14}$TFSI-based composite cathode tape comprising $Li(Ni_{0.8}Co_{0.15}Al_{0.05})O_2$ (NCA) as active material; Panel A: Top-view onto the composite cathode tape, magnification 500×, the enlargement shows an NCA particle that is embedded in the polymer electrolyte fraction, magnification 12,000×. Panel B: Cross-sectional view of the composite cathode tape, magnification 1000×. Electron acceleration voltage: 1.00 kV.

force that was exerted on the large secondary NCA particles at the surface of the tape during cold-calendaring was indeed strong enough to break the secondary particle, however, it was not sufficient to break the secondary NCA particles within the cathode bulk, which are embedded in a thick shell of polymer electrolyte. As a consequence, the relative NCA particle/polymer electrolyte interface is reduced, which results in an inferior rate capability and utilized capacity of the composite cathode due to the slower lithium ion bulk diffusion in the NCA particles, compared to the polymer electrolyte fraction.

3.3. Thermal properties of the composite cathodes

Due to the absence of volatile and highly flammable liquid compounds, lithium metal polymer batteries promise significantly improved safety characteristics compared to conventional liquid alkyl-carbonate-based electrolytes. However, to exclude safety issues related to eventual hazardous side reactions in presence of 4 V-class active materials at elevated temperature, the composite cathodes were evaluated in terms of their thermal stability. For comparison reasons, LiFePO$_4$ as already established 3 V-class cathode active material was also investigated. Hence, thermogravimetric analysis (TGA) and differential scanning calorimetry (DSC) were performed to investigate the sample mass loss and heat flow as a function of the temperature.
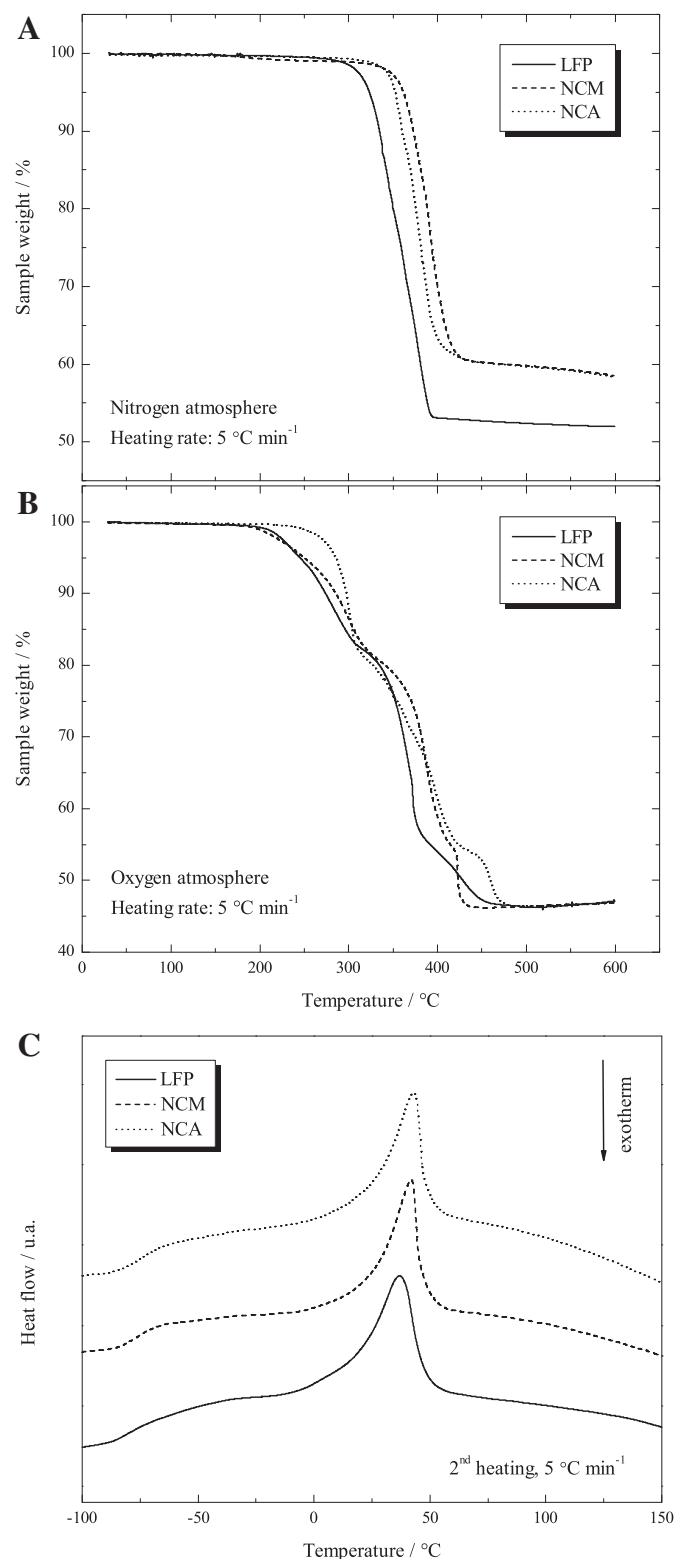
Fig. 3. Thermogravimetric analysis (TGA) traces of different PEO-LiTFSI-Pyr$_{14}$TFSI-based composite cathode tapes, comprising LFP, NCM or NCA as active material, as a function of the temperature in nitrogen atmosphere (Panel A) and oxygen atmosphere (Panel B), respectively. Heating rate: 5 °C min^{-1}. Panel C: Differential scanning calorimetry (DSC) heating traces of different PEO-LiTFSI-Pyr$_{14}$TFSI-based composite cathode tapes, comprising either LFP, NCM or NCA as active material, in nitrogen atmosphere, using a heating rate of 5 °C min^{-1}.

Fig. 3 shows the TGA traces of the composite cathodes obtained in nitrogen (Panel A) and oxygen atmosphere (Panel B). In agreement with previous investigations on PEO-LiTFSI-Pyr$_{14}$TFSI ternary SPEs, the TGA curves of the composite cathodes in nitrogen atmosphere in Fig. 3 (Panel A) indicated a one-step decomposition mechanism [33]. Table 1 summarizes the thermal properties of the composite cathodes, including the decomposition temperatures T_{dec}. For comparison reasons, the T_{dec} of the pure PEO-LiTFSI-Pyr$_{14}$TFSI (20/1/4) solid polymer electrolyte, whose mole ratio corresponds to the composition of the polymer electrolyte fraction in the composite cathodes, is also listed. Accordingly, the T_{dec} of the ternary SPE in nitrogen atmosphere is about 278 °C, which matches with the T_{dec} of the LFP-based composite cathode ($\sim$275 °C). Interestingly, the 4 V-class composite cathodes exhibit higher T_{dec} (above 310 °C) than the LFP-based composite cathode. The cause for the lower thermal stability of the LFP-based composite cathode is most likely related to the higher surface area of this active material.

Additionally, LFP particles are coated by carbon, which is assumed to have a catalytic effect on the decomposition of the PEO-based polymer electrolyte fraction, the lower T_{dec} of the LFP-based composite cathode presumably results from an increased accessible surface area of catalytic active carbon [12].

In agreement with Fig. 3 (Panel A), the catalytic effect of LFP nano material is also reflected by the relative mass loss and the residual mass of the investigated composite cathodes. Since the one-step decomposition mechanism can be ascribed to the decomposition of PEO (17.5 wt%), LiTFSI (5 wt%) and Pyr$_{14}$TFSI (27.5 wt%), a relative mass loss of about 50 wt% would have been expected. However, in case of the previously described ternary SPEs it was observed that upon heating up to 600 °C, a residual between 10 and 15 wt% remained, which corresponds to an overall residue of at least 60 wt% in the derivate composite cathode (43 wt% active material, 7 wt% carbon, 10 wt% residual). However, in contrast to the 4 V-class composite cathodes, the decomposition of the LFP-based composite cathode is additionally facilitated by higher accessibility of catalytic carbon surface and lower rigidity of the sample, so that the amount of residue is significantly reduced by 13 wt%, corresponding to 54 wt% remaining sample weight after completion of the one-step decomposition mechanism.

Fig. 3 (Panel B) shows the TGA traces of the composite cathodes in oxygen atmosphere. Accordingly, all samples indicated a three-step decomposition mechanism that can be ascribed to a step-wise, though partially overlapping decomposition of PEO, LiTFSI, Pyr$_{14}$TFSI, and carbon. The corresponding mass loss during each stage was about 18 wt%, 27 wt%, and 8 wt%, which perfectly matches with the initial cathode composition of PEO (17.5 wt%), LiTFSI, Pyr$_{14}$TFSI (5 + 27.5 wt%), and carbon (7 wt%). The remaining sample weight after completion of the mechanism is 47 wt%, including the active material (43 wt%), as well as few residual and possible oxygen uptake at high temperatures. Since the deviation of the LFP trace and the 4 V-class composite cathodes was much smaller as in nitrogen atmosphere, it becomes clear that the effects related to the available carbon surface are less distinctive in oxygen

Table 1
Thermal properties of the PEO-LiTFSI-Pyr$_{14}$TFSI-based composite cathodes. The data from the pure P(EO)$_{20}$LiFSI-(Pyr$_{14}$TFSI)$_4$ solid polymer electrolyte were taken from Ref. [34].

Cathode active material	T_{dec} in N$_2$/°C	T_{dec} in O$_2$/°C	T_g/°C	T_m/°C	ΔH_m/J g^{-1}
P(EO)$_{20}$LiTFSI-(Pyr$_{14}$TFSI)$_4$	278	175	−71	50.8	−19
LiFePO$_4$	275	180	−78.5	36.8	−7.8
Li(Ni$_{1/3}$Co$_{1/3}$Mn$_{1/3}$)O$_2$	315	180	−74.9	41.9	−7.3
Li(Ni$_{0.8}$Co$_{0.15}$Al$_{0.05}$)O$_2$	310	215	−74.6	43.0	−7.4

atmosphere. Though the onsets of the decomposition mechanisms differ in the range from 180 °C to 215 °C, which may also be associated to individual morphological changes upon temperature treatment and possible phase transitions in the active materials [35], all composite cathodes indicated no remarkable features up to the melting temperature of lithium at about 180 °C.

Nevertheless, besides the differences between the LFP-based and 4 V-class composite cathodes it is remarkable that the composite cathodes perform equal or even higher thermal stabilities compared to the pure ternary SPE both in nitrogen and oxygen atmosphere. As a result of the previously discussed detrimental effects related to the presence of catalytic carbon, it would have been expected that the thermal stabilities decrease upon addition of the cathode active material and carbon. However, the results listed in Table 1 indicate the presence of an additional influence factor that counterbalances and/or even partially eliminates these effects. Considering that the cathode active particles and the conductive carbon form a continuous network throughout the composite, which might ambivalently acts on the one hand as a plasticizer that improves the mobility within the polymer matrix, and on the other hand as a buffer that slows down the decomposition kinetics. A similar ambivalent phenomenon may be ascribed to $Pyr_{14}TFSI$. While the addition of ionic liquid increases the softness of the composite, thus facilitating the decomposition kinetics, the presence of thermal and electrochemical highly stable ionic liquid may also give a beneficial impact at the interfaces between the polymer electrolyte fraction and the carbon as well as cathode active material particles. There, the ionic liquid is expected to protect the components from detrimental interaction, including PEO decomposition due to catalysis at the carbon surface or contact with the active material.

As a consequence the thermal stabilities of the PEO-LiTFSI-$Pyr_{14}TFSI$-based composite cathodes (see Table 1) were well above the boiling and decomposition temperatures of conventional liquid alkyl-carbonate-based electrolytes, thus making them very suitable for application in lithium metal polymer batteries. Nevertheless, it is to note that the decomposition temperature of 4 V-class composite cathodes in the delithiated (charged) state could be further decreased, however, the much slower exothermal decomposition kinetics and the absence of volatile components still significantly reduce the risk of thermal runaway and cell explosion.

Fig. 3 (Panel C) shows the DCS traces of the 2nd heating scan for the composite cathodes. As it can be seen, all samples indicated a quite similar behavior, including a glass transition and a broad endothermic feature that can be associated with the melting of crystalline PEO and PEO:LiTFSI phases. The glass transition temperatures T_g, the melting temperatures T_m, as well as the melting enthalpies ΔH_m are summarized in Table 1.

Accordingly, the addition of the electrode fraction (43 wt% active material and 7 wt% carbon) into the PEO-LiTFSI-$Pyr_{14}TFSI$ polymer electrolyte fraction resulted in a shift of T_g, T_m and ΔH_m to substantially lower values, whereby, except the melting enthalpy, the impact is more effective in the LFP-based composite cathode. While the pure ternary polymer electrolyte fraction (20/1/4) indicated a glass transition at −71 °C and melting peak at 50.8 °C, the 4 V-class composite cathodes showed a T_g at about −75 °C and a T_m around 43 °C. The LFP-based composite cathode, however, exhibited a T_g at −78.5 °C and a T_m at 36.8 °C. In terms of melting enthalpy, the addition of the electrode fraction caused a decline from −19 J g^{-1} in the pure ternary polymer electrolyte fraction to about −7.5 J g^{-1} in the composite cathodes. Considering that the glass transition is an intramolecular interaction, at which the mobility of molecular groups within the amorphous phase of the polymer progressively increases, e.g. by overcoming of rotation barriers, the electrode active material fraction acts as a solid plasticizer that kinetically

prevents the crystallization of PEO [36]. As a consequence, the addition of the electrode fraction favors the amorphicity and mobility within the polymer electrolyte fraction, thus increasing the softness of the derivative composite cathode. An analogous, plasticizing behavior was reported for an increasing amount of either ionic liquid or certain ceramic fillers into a PEO-based solid polymer electrolyte [33,37]. The origin of this phenomenon is closely related to the morphology and the size of the active material particles, thus causing a larger impact of the comparatively smaller LFP particles on the T_g and T_m of the derivative composite cathode.

It is to note that although the melting temperature of the composite cathodes is very close to the provided operating temperature of 40 °C in the Li/SPE/cathode batteries, no substantial change in the mechanical properties could be observed, because the endothermic peaks were suggested to result from dissolution of crystalline parts into a purely amorphous phase [38]. In agreement with the TGA traces, no further thermal features could be observed up to 150 °C, thus proving the absence of eventual decomposition reactions.

3.4. Li/SPE/cathode battery performance

Fig. 4 shows the battery performance of the Li/P(EO)$_{10}$LiTFSI-$(Pyr_{14}TFSI)_2$/cathode lithium metal polymer batteries, obtained by galvanostatic cycling at 40 °C. The cut-off potentials were set to 3.0 V during discharge and 4.0 V for LiFePO$_4$ (theoretical capacity: 170 mAh g^{-1}) or 4.3 V for Li(Ni$_{1/3}$Co$_{1/3}$Mn$_{1/3}$)O$_2$, Li(Ni$_{0.8}$Co$_{0.15}$Al$_{0.05}$)O$_2$ (specific capacities: 160 mAh g^{-1} and 190 mAh g^{-1}, respectively) during charge to gain high capacity utilization.

In agreement with recently reported results, the 3 V-class Li/SPE/LFP battery showed high capacity utilization of about 161 mAh g^{-1} and excellent capacity retention upon cycling [39]. The 4 V-class Li/SPE/NCM and Li/SPE/NCA batteries, however, also delivered high initial capacities of about 157 mAh g^{-1} (NCM) and 185 mAh g^{-1} (NCA), but suffered a significant decline in capacity by increasing the current density from 0.04 mA cm^{-2} (C/20) to 0.08 mA cm^{-2} (C/10). Considering the scanning electron microscopy images of the NCA composite cathode, the latter behavior may be explained by insufficient disaggregation of the secondary
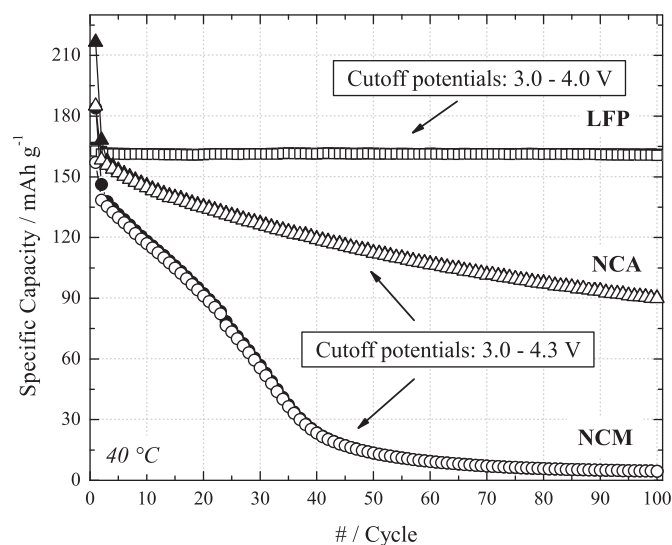

Fig. 4. Capacity vs. number of cycle of Li/SPE/cathode lithium metal polymer batteries (solid marker: charge, empty marker: discharge), comprising either LFP, NCM or NCA as cathode active material, obtained at 40 °C. Electrochemical active area: 1.13 cm^2, mass loading: 4–5 mg, initial current density 0.04 mA cm^{-2} (C/20), subsequent cycles 0.08 mA cm^{-2} (C/10).

cathode active material particles during cold-calendaring. As a consequence, the average diameter of NCM and NCA particles (~5 μm) is much larger than that of LFP particles (200–300 nm), resulting in a lower rate capability. In the subsequent cycles, the Li/SPE/NCM battery exhibited a significant and progressive decrease in capacity, leading to cell failure after 40 cycles. In contrast, the Li/SPE/NCA battery indicated a regressive and overall smaller capacity fading with about 60% capacity retention after 100 cycles at C/10.

Accordingly, the 4 V-class Li/SPE/cathode lithium metal polymer batteries indicated high initial capacities, but also suffer a significant reduction in rate capability and capacity retention when compared to the 3 V-class Li/SPE/LFP battery. However, the causes of this phenomenon may not only be ascribed to the higher operating potential, because both 4 V-class cathode active materials displayed different degradation mechanisms, indicating an active material-specific dependence. While the NCM cathode active material is still subject to future investigation, in the following, the degradation mechanism of NCA as initially more attractive 4 V-class cathode active material was investigated in terms of the interfacial properties of the Li/SPE/NCA battery.

3.5. Interfacial properties of Li/SPE/Li(Ni$_{0.8}$Co$_{0.15}$Al$_{0.05}$)O$_2$ batteries

Symmetrical Al^0/cathode/SPE/cathode/Al^0 and Li/SPE/Li cells were assembled to investigate the chemical stability of the solid polymer electrolyte (SPE) in presence of uncharged 4 V-class composite cathodes, incorporating Li(Ni$_{0.8}$Co$_{0.15}$Al$_{0.05}$)O$_2$ as active material, and lithium metal, separately. Fig. 5 shows the time dependence of the AC impedance responses of these cells, thereby, each cell indicated a distorted semicircle, which is associated with the electrode interfacial resistance ($R_{cathode, int}$ and $R_{Li/SPE, int}$, respectively). The intercept with the Z'-axis at high frequencies can be ascribed to the polymer electrolyte ionic bulk resistance $R_{SPE, bulk}$, while in the low frequency region of the Al^0/cathode/SPE/cathode/Al^0 cell the semicircle is followed by a 45° linear slope that accounts for the Warburg diffusion impedance $Z_{Warburg}$, and then, an inclined straight line toward the Z'-axis, which displays the cathode limit capacitance C_{lim} [40]. The impedance data were analyzed by a nonlinear least square (NLLS) fit software, using a proper equivalent electric circuit, which is depicted in Fig. 5 (Panel C) [41,42]. However, for the fitting of the symmetrical Li/SPE/Li cells the Warburg diffusion impedance as well as the cathode limit capacitance were not considered because the effect of these two elements were not observed in the spectra (Fig. 5, Panel D).

As shown in Fig. 5 (Panel A), the $R_{SPE, bulk}$ and the $R_{cathode, int}$ remained stable for almost two months at values of 7 ± 1 Ω cm^2 and 34 ± 2 Ω cm^2, respectively, thereby exhibiting only marginal increase of few Ω cm^2, which is a strong evidence for the chemical stability of the uncharged 4 V-class composite cathode system at open circuit conditions.

It is important to stress, that the cathode interfacial resistance not only comprises the cathode/polymer electrolyte interface but also the cathode/Al^0 interface. As a consequence, both interfaces have to be taken into account. In terms of the cathode/Al^0 interface it is well known that despite its low Al/Al^{3+} oxidation potential of 1.39 V vs. Li/Li$^+$, metallic aluminum typically indicates an extraordinary kinetic stability, which is caused by a spontaneous protective oxide surface film growth [43]. In addition, the Al^{3+} ions are not soluble in PEO, thus even in presence of LiTFSI the aluminum is almost resistant to uniform corrosion at current densities as small as <0.05 mA cm^{-2} during potentiodynamic or potentiostatic anodic polarization at moderate potentials <3.8 V vs. Li/Li$^+$ [44]. However, in terms of higher current densities and higher potentials occurring during battery cycling, the aluminum is increasingly susceptible to pitting corrosion that arises from local breakdown of the protective
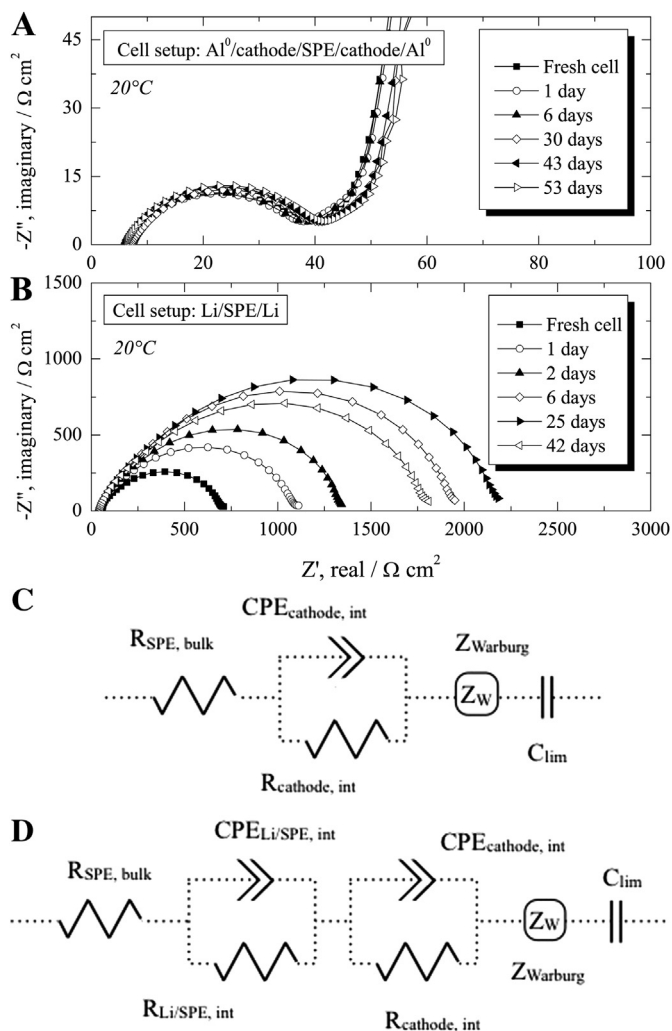

Fig. 5. AC impedance responses of symmetrical Al^0/cathode/SPE/cathode/Al^0 (Panel A) and Li/SPE/Li (Panel B) cells, respectively, as a function of the time, that were obtained at 20 °C. The cathode active material was Li(Ni$_{0.8}$Co$_{0.15}$Al$_{0.05}$)O$_2$. Frequency range: 65 kHz–100 mHz. Equivalent circuit models, that were used for the analysis of the AC impedance responses of the symmetrical Al^0/cathode/SPE/cathode/Al^0 cells (Panel C) and asymmetrical Li/SPE/cathode batteries (Panel D).

film due to locally higher current densities at the points of contact between active material particles in the composite cathode and the aluminum current collector surface [45]. With respect to Fig. 5 (Panel A) it can be reasoned that at open circuit conditions in presence of the uncharged 4 V-class cathode active material, the aluminum current collector does not show remarkable corrosion when in contact with the PEO-LiTFSI-Pyr$_{14}$TFSI-based composite cathode.

The three-dimensional f–Z'–Z'' plot in Fig. 6 summarizes the frequency dependence of the impedance responses of an asymmetrical Li/SPE/cathode cell and two symmetrical Li/SPE/Li and cathode/SPE/cathode cells, respectively (cathode active material: Li(Ni$_{0.8}$Co$_{0.15}$Al$_{0.05}$)O$_2$).

In agreement with previous investigations on Li/SPE/LFP lithium metal polymer batteries [39], the shape and the extend of the impedance response of the present Li/SPE/NCA cell is mainly characterized by the interfacial resistance which is associated with the lithium/polymer electrolyte interface $R_{Li/SPE, int}$. Considering that about 90% of $R_{Li/SPE, int}$ can be ascribed to the impedance, arising from lithium ion migration through the protective film on the lithium surface $R_{Li/SPE,pas}$, it can be deduced that the overall
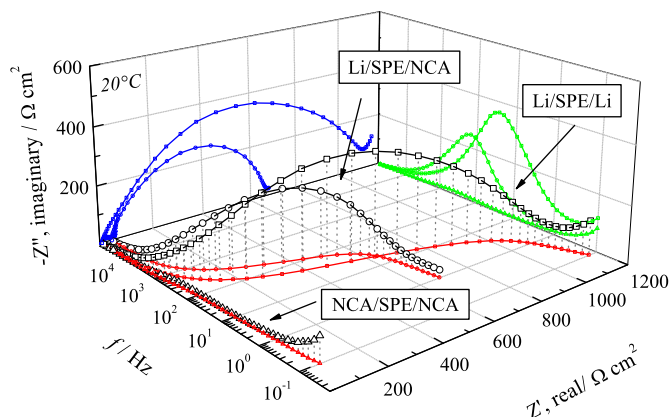
Fig. 6. Frequency dependence of the impedance response of an asymmetrical Li/SPE/cathode cell (squares), a symmetrical Li/SPE/Li cell (circles), and a symmetrical cathode/SPE/cathode cell (triangles), obtained at 20 °C after annealing for 1 day at room temperature, normalized to the electrochemical active area. The cathode active material was Li(Ni$_{0.8}$Co$_{0.15}$Al$_{0.05}$)O$_2$. Frequency range: 65 kHz–100 mHz.

battery impedance almost fully originates from the polarization of the protective film on the lithium electrode surface. However, the asymmetric shape of the Li/SPE/cathode and Li/SPE/Li impedance response support the existence of another impedance contribution, which is known as charge-transfer resistance at the lithium/polymer electrolyte interface $R_{Li/SPE, ct}$ ($R_{Li/SPE, int} = R_{Li/SPE,pas} + R_{Li/SPE, ct}$) [46,47]. As shown in Fig. 5 (Panel B) the $R_{Li/SPE, int}$ increased remarkably during the initial storing period, but leveled at about 1750 Ω cm^2 after one month of storage, when the thickness of the protective film prevents the lithium metal from further reaction with polymer electrolyte [34].

Although the contribution of the cathode interfacial resistance $R_{cathode, int}$ to the Li/SPE/cathode impedance response took only minor impact on the overall resistance, Fig. 6 indicates, that the serial extension of the lithium/polymer electrolyte interface by a polymer electrolyte/cathode/Al^0 segment increased the distortion of the semicircle, which corresponds to a less ideal behavior of the circuit elements involved. The causes for this phenomenon may include electrode surface roughness, e.g. at the cathode/Al^0 interface, as well as inhomogeneity arising from locally varying composition of the composite cathode. By modeling the interfacial processes related to each electrode with a Cole–Cole element, comprising a constant phase element, the AC impedance response of the Li/SPE/cathode battery was analyzed according to the equivalent circuit model described in Fig. 5 (Panel D) [40,48].

$$f_{max} = \frac{1}{2\pi\tau} = \frac{1}{2\pi RC} \qquad (1)$$

$$L \propto \sqrt{D\tau} \qquad (2)$$

In agreement with the results obtained for symmetrical cells depicted in Fig. 5, the Li/SPE/NCA batteries revealed a $R_{SPE, bulk}$ of 11.2 Ω cm^2, a $R_{Li/SPE, int}$ of 765 Ω cm^2, and a $R_{cathode, int}$ of 37.7 Ω cm^2 after 1 day of storage at 20 °C, thus confirming the assumption, that the overall impedance is almost fully located at the lithium/polymer electrolyte interface. In addition, the peak frequency f_{max} of the large semicircle of the Li/SPE/NCA full battery was shifted to lower frequencies by about one order of magnitude compared to the symmetrical cells. As a consequence, according to Eq. (1) the distribution of relaxation time constants τ broadened and was shifted to higher values, which could be explained by different thicknesses of the polarized interfacial films (diffusion thickness L) and/or

different lithium diffusion coefficients D at the electrode/polymer electrolyte interfaces, as described by Eq. (2) [49]. Taking into account the cathode interfacial resistance in Fig. 5, these results may indicate the presence of a surface film besides the charge-transfer resistance at the cathode/polymer electrolyte interface, which hampers the migration of lithium ions. To investigate the origins of this phenomenon, Li/SPE/NCA batteries were cycled to different anodic cut-off potentials in order to study the influence of the applied potential on the delivered capacity and cyclability of the 4 V-class composite cathodes.

3.6. Degradation behavior of Li/SPE/Li(Ni$_{0.8}$Co$_{0.15}$Al$_{0.05}$)O$_2$ batteries

Fig. 7 shows the initial cell potential vs. specific capacity profiles of the Li/SPE/NCA lithium metal polymer batteries, which were operated at different anodic cut-off potentials ranging from 4.0 V to 4.45 V. Accordingly, all profiles indicated the same inclined curve that is also commonly observed in conventional Li-ion batteries utilizing Li(Ni$_{0.8}$Co$_{0.15}$Al$_{0.05}$)O$_2$ cathodes with alkyl-carbonate-based electrolyte solutions [50]. As a consequence of the decrease in the anodic cut-off potential, the cell potential profiles gradually shifted in parallel to lower delivered capacities. Nonetheless, the present all-solid-state lithium metal polymer batteries delivered remarkable initial capacities between 120 mAh g^{-1} (3.0–4.0 V) and 185 mAh g^{-1} (3.0–4.45 V) at an operating temperature as low as 40 °C.

Fig. 8 (Panel B) shows the cyclic performance of the Li/SPE/NCA lithium metal polymer batteries operating at different anodic cut-off potentials at 40 °C, according to which the delivered capacity and its evolution upon cycle number was greatly influenced by the anodic cut-off potential. Apparently, the extended anodic cut-off potential displayed a trade-off between a beneficial enhancement of the delivered capacity and an increased capacity fading upon cycling, which is a considerable threat to continuous battery operation. In agreement with the results obtained for the Li/SPE/NCA battery illustrated in Fig. 4, all batteries indicated a regressive capacity fading behavior, although the recovery rate was greatly influenced by the anodic cut-off potential. Accordingly, the first cycles were mainly characterized by activation processes in the
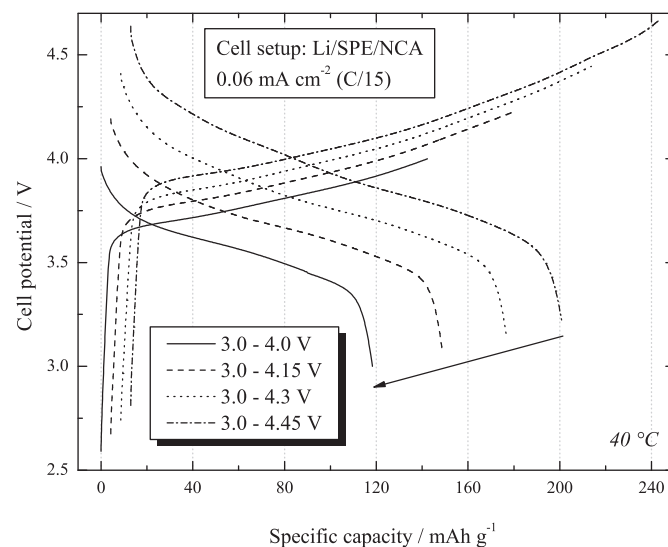

Fig. 7. Waterfall plot of the cell potential vs. specific capacity profiles of the first charge–discharge cycles of Li/SPE/NCA lithium metal polymer batteries, operating at different anodic cut-off potentials. Temperature: 40 °C, current density: 0.06 mA cm^{-2} (C/15).
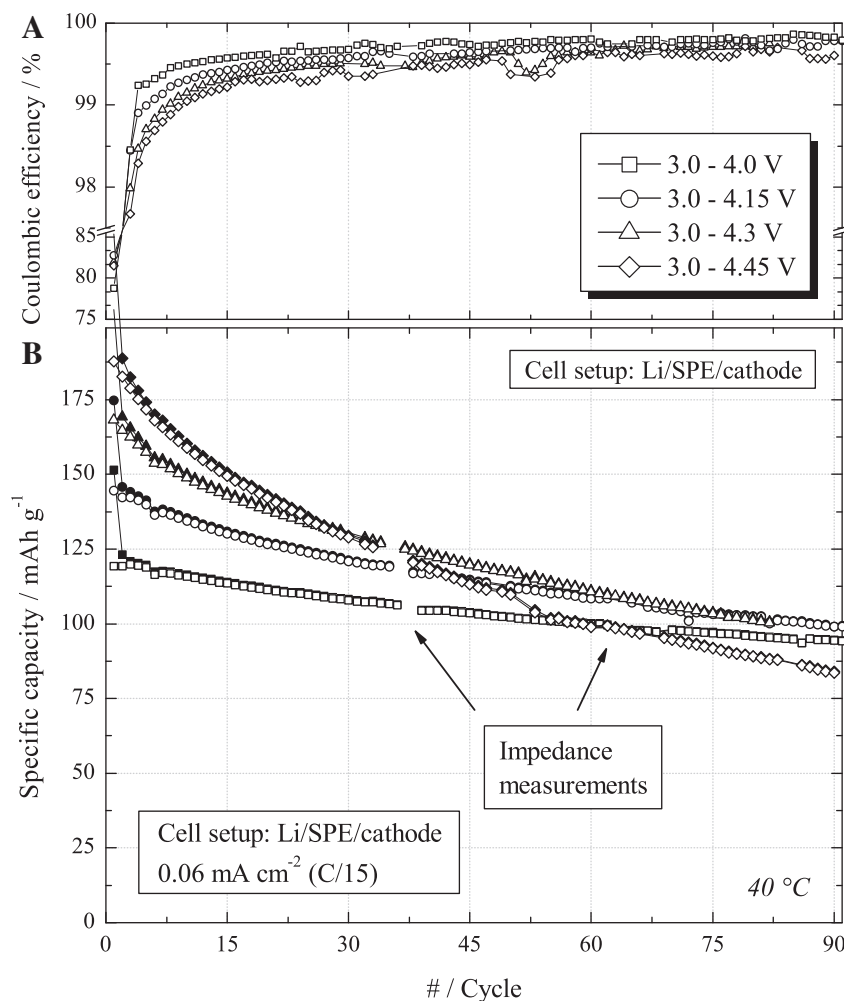
Fig. 8. Coulombic efficiencies (Panel A) and cyclic performance (Panel B) for Li/SPE/NCA lithium metal polymer batteries (solid marker: charge, empty marker: discharge), operating at different anodic cut-off potentials between 3.0 V during discharge and 4.0 V, 4.15 V, 4.3 V, and 4.45 V during charge, respectively. Temperature: 40 °C, current density 0.06 mA cm^{-2} (C/15).

cathode material and passivation phenomena at the electrode/polymer electrolyte interfaces, whose extend greatly depended on the anodic cut-off potential. The charge–discharge efficiencies upon battery cycling, which are shown in Fig. 8, support this assumption. It can be seen, that in the first cycle all batteries indicated a coulombic efficiency as low as 80%, which can mainly be ascribed to side reactions occurring at the interface of the polymer electrolyte and the 4 V-class composite cathodes. In contrast, previous 3 V-class Li/SPE/LFO full batteries only exhibited an initial irreversible capacity loss of less than 2%. However, starting from the second cycle the coulombic efficiencies of the Li/SPE/NCA batteries asymptotically increased up to values ranging between 99.5 and 99.75%, whereby a strong but decreasing dependence on the anodic cut-off potential could be observed.

Interestingly, the Li/SPE/NCA batteries that were cycled between cut-off potentials of 3.0 V–4.0 V also showed a slight average capacity fading of about 0.3% per cycle, whereas the Li/SPE/LFP battery in Fig. 4, operating at the same conditions, indicated no remarkable degradation up to 100 cycles. As a consequence, even in absence of high anodic cut-off potentials, the utilization of a 4 V-class cathode active material caused additional degradation that could not be observed while utilizing a 3 V-class composite cathode. During the first cycles these may be dominated by the formation of a surface film at the cathode/polymer electrolyte

interface and corrosion of the aluminum current collector due to local breakdown of the protective film upon current flow through the cell in presence of the 4 V-class cathode active material, whereas in the subsequent cycles the ongoing capacity fading can rather be ascribed to irreversible structural changes in the cathode active material, residual aluminum corrosion, and electric contact losses at the cathode/Al^0 interface [17,51]. To study the influence of the anodic cut-off potential on these processes and identify eventual interdependencies, impedance measurements were carried out after selected cycles.

Fig. 9 illustrates the evolution of the impedance spectra for the Li/SPE/NCA lithium metal polymer cells upon galvanostatic cycling at different anodic cut-off potentials at 40 °C. The initial overall impedance after 1 day of storage at 20 °C, but prior to galvanostatic cycling, was about 850 Ω cm^2. Referring to the 3-D plot in Fig. 6, the Li/SPE/cathode battery AC impedance response exhibited a distorted semicircle that consisted of a distribution of relaxation time constants associated with the electrode/polymer electrolyte and cathode/Al^0 interfacial resistances. In the subsequent cycles, the cell impedance indicated a significant growth that was greatly influenced by the anodic cut-off potential. For comparison reasons, the battery impedance and corresponding delivered capacities, as well as the capacity retention of selected cycles are listed in Table 2.
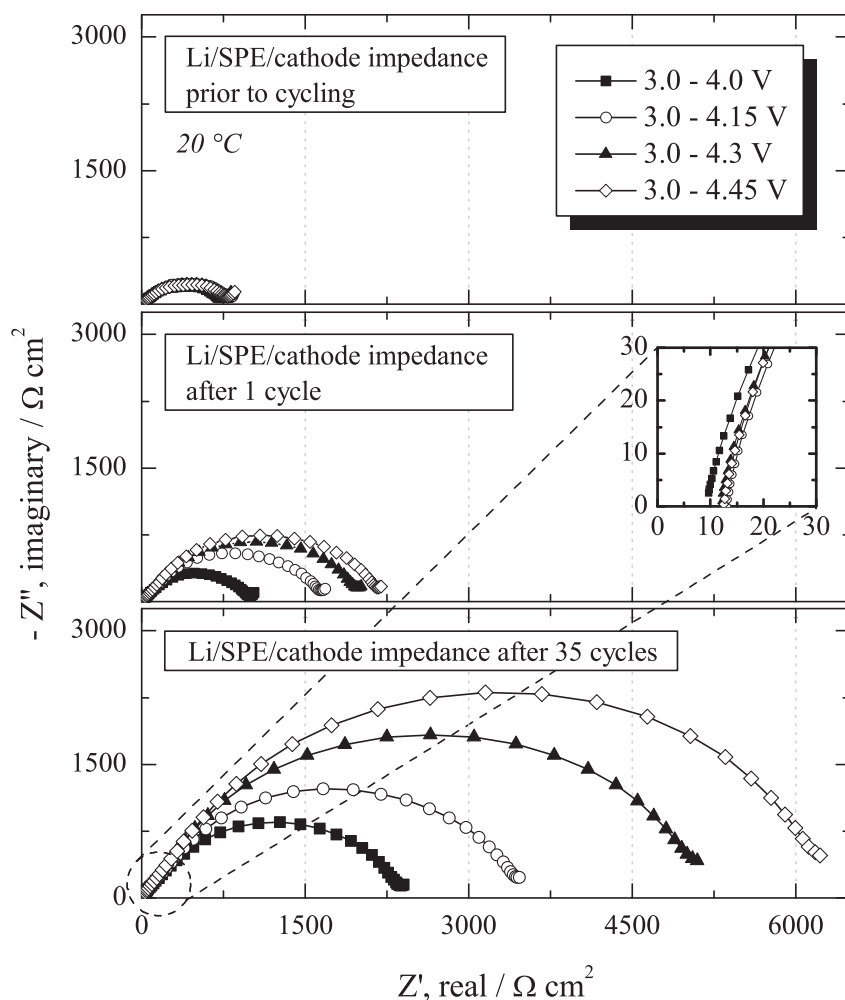
Fig. 9. Impedance evolution for Li/SPE/NCA lithium metal polymer batteries upon galvanostatic cycling at different anodic cut-off potentials. The measurements were performed prior to cycling, after 1 cycle, and after 35 cycles. Temperature: 20 °C. Frequency range: 65 kHz–100 mHz.

Accordingly, as soon as current flowed through the cell during battery operation between cut-off potentials of 3.0 and 4.0 V, the battery impedance increased to about $R_{battery} = 2380 \, \Omega \, cm^2$ after 35 cycles. Taking into account lithium stripping-plating tests of symmetrical Li/SPE/Li cells and subsequent AC impedance measurements after selected cycles, which are illustrated in Fig. 10, it can be deduced, that the growth of the protective surface film associated with the lithium/polymer electrolyte interface was completed at that time. The corresponding interfacial resistance contribution leveled at about $R_{Li, int} = 1850 \, \Omega \, cm^2$. Consequently, even after 35 charge–discharge cycles between 3.0 and 4.0 V, the cathode interfacial resistance still contributed less than 23% to the overall battery impedance ($R_{battery} = R_{SPE, bulk} + R_{Li, int} + R_{cathode, int}$). However, with increasing anodic cut-off potential the contribution rapidly grew to about 65% (3.0–4.3 V) and even more than 70% (3.0–4.45 V), which corresponded to an increasing capacity fading as depicted in Fig. 8. In this context, the cut-off potential-dependent contribution of the cathode interfacial resistance $R_{cathode, int}$ may be explained on the one hand by the formation of a surface film at the cathode/polymer electrolyte interface and on the other hand by aluminum corrosion occurring at the cathode/Al^0 interface.

In terms of the cathode/polymer electrolyte interface it is assumed, that the surface film, which is believed to be formed at the interface, behaved in a similar way as does the lithium/polymer electrolyte protective film, so that it grows until a certain thickness is reached, thus protecting the polymer electrolyte toward further reaction with the 4 V-class cathode active material. Thereby, Figs. 8–10 indicated that the cathode/polymer electrolyte surface film growth rate as well as its final thickness greatly depended on the anodic cut-off potential and the presence of current flow through the cell. In agreement with the assumption of a finite surface film formation, no remarkable continuous decomposition of the PEO-LiTFSI-Pyr$_{14}$TFSI polymer electrolyte could be observed, as it shown by the extraordinary stable $R_{SPE, bulk}$, which is depicted in the enlargement in Fig. 9.

Analogously, in agreement with recent investigations on the corrosion behavior of the aluminum current collector in contact

Table 2
Comparison of the delivered capacity, capacity retention, and battery impedance for selected cycles for the Li/SPE/NCA lithium metal polymer batteries, operating at different anodic cut-off potentials at 40 °C. The impedance measurements were performed at 20 °C.

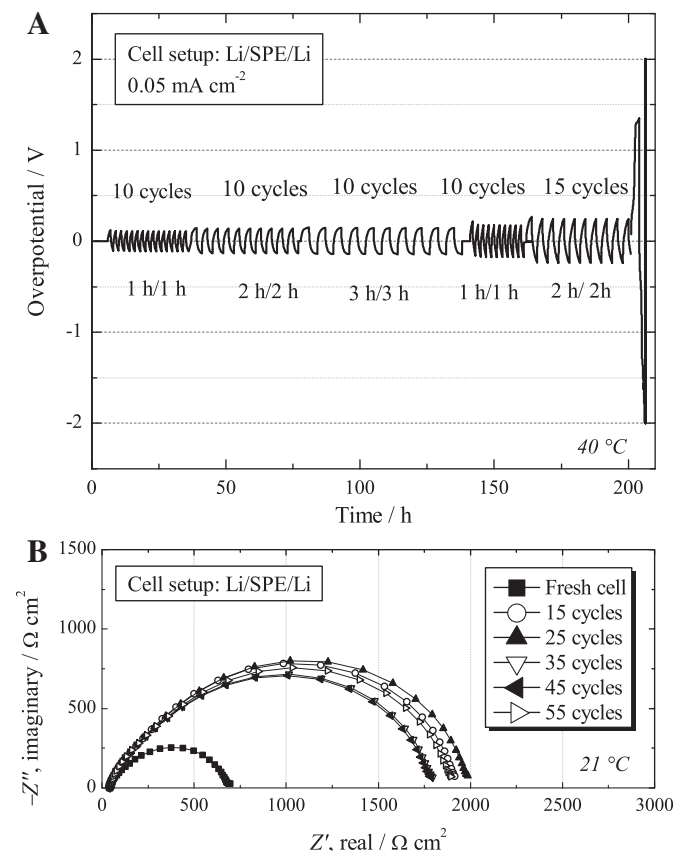| Cut-off potential/V	Delivered capacity/ mAh g^{-1}		Capacity retention/%	Battery impedance/ Ω cm^2	
	1 Cycle	35 Cycles		1 Cycle	35 Cycles
3.0–4.0 V	119	107	89.9	960	2380
3.0–4.15 V	145	119	82.1	1620	3450
3.0–4.3 V	168	126	75.0	1990	5160
3.0–4.45 V	186	125	67.2	2170	6390

A

B

Fig. 10. Evolution of the overpotential for a symmetrical Li/SPE/Li cell with different galvanostatic polarization pulse times, using a constant current of 0.05 mA cm^{-2} at 40 °C (Panel A), and subsequent AC impedance measurements after selected cycles. Frequency range: 65 kHz–100 mHz (Panel B).

with LiTFSI-containing PEO-based polymer electrolytes, the impedance evolution in Fig. 9 indicates that the corrosion rate was also strongly related to the applied potential [45]. Accordingly, at higher potentials, the protective surface film at the aluminum was increasingly susceptible to breakdown, resulting from local high current densities, thus enabling corrosion at the spots of metallic aluminum surface. Hence, Yang et al. proposed a corrosion mechanism, according to which the dissolution of aluminum into LiTFSI-based electrolytes involves the formation of Al-TFSI complexes at the blank aluminum surface, followed by subsequent dissolution and diffusion of Al(TFSI)$_3$ into the electrolyte solution [52]. In contrast to previous literature, where an aluminum dissolution potential of about 3.8 V vs. Li/Li$^+$ was observed for PEO-LiTFSI polymer electrolytes [44], Garcia et al. suggested that the presence of an ionic liquid, providing the same anion, effectively diminished the dissolution of Al(TFSI)$_3$ into the electrolyte [53], thus shifting the aluminum dissolution potential to higher values [54,55]. As a consequence, it can be reasoned that although the cathode/Al^0 interfacial resistance is increasingly susceptible to pitting corrosion upon increasing anodic cut-off potential, it also benefits from the presence of Pyr$_{14}$TFSI and the insolubility of Al^{3+} ions in PEO, thus allowing adequate battery performance even at potentials as high as 4.3 V.

Interestingly, except the Li/SPE/NCA battery running up to 4.45 V, the regressive capacity fading in Fig. 8 as well as the increasing coulombic efficiencies in Fig. 8 indicated an at least partial stabilization of the degradation processes, occurring during the initial phase of battery cycling. In terms of a possible

protective film at the cathode/polymer electrolyte interface this may result from completed growth, thus inhibiting further reaction, whereas the pitting corrosion at the aluminum current collector may increasingly be diminished by the insolubility of the Al(TFSI)$_3$ corrosion products into the Pyr$_{14}$TFSI-containing polymer electrolyte fraction in the composite cathode. In contrast, the ongoing capacity fading upon galvanostatic cycling can be ascribed to irreversible structural changes, which are also reported for conventional Li(Ni$_{0.8}$Co$_{0.15}$Al$_{0.05}$)O$_2$ cathodes in liquid electrolyte solutions (EC-DMC-1 M LiPF$_6$), as well as remaining aluminum corrosion, deformation and loss of electric contact at the cathode/Al^0 interface. It is to note, that subsequent impedance measurements after 60 cycles (not shown) revealed only marginal ongoing increase of the overall battery impedance of Li/SPE/NCA batteries running at anodic cut-off potentials as high as 4.3 V, thus confirming the conclusion that the initial large increase of the battery impedance is mainly attributed to passivation phenomena at the electrode/polymer electrolyte interfaces and aluminum corrosion, rather than to continuous polymer electrolyte decomposition.

4. Conclusions

PEO-LiTFSI-Pyr$_{14}$TFSI-based 4 V-class composite cathodes, incorporating either Li(Ni$_{1/3}$Co$_{1/3}$Mn$_{1/3}$)O$_2$ or Li(Ni$_{0.8}$Co$_{0.15}$Al$_{0.05}$)O$_2$, were prepared by a hot-pressing process, which showed excellent mechanical stability and flexibility. Thermal investigations revealed equal or even higher thermal stabilities of the composite cathodes when compared to corresponding pure solid polymer electrolytes, thereby showing no decomposition features at least up to 180 °C in oxygen atmosphere. However, TGA and DSC measurements demonstrated an ambivalent influence of the active material-carbon electrode fraction on the thermal properties of the polymer electrolyte fraction in terms of amorphicity, mobility and decomposition kinetics.

The battery performance of truly dry, all-solid-state 4 V-class Li/SPE/cathode lithium metal polymer batteries revealed high initial capacity utilization, but also much lower capacity retention compared to the 3 V-class composite cathodes, hence, different degradation mechanisms could be observed for NCM and NCA. Subsequent in-depth investigation of the Li/SPE/NCA interfacial properties and battery performance indicated a strong dependence of the electrochemical properties on the anodic cut-off potential and the presence of current flow through the cell. Accordingly, at open circuit conditions the uncharged composite cathode was chemical stable in presence of the solid polymer electrolyte and the aluminum current collector, whereas during the first cycles of battery operation the overall battery impedance was mainly characterized by finite passivation phenomena at the electrode/polymer electrolyte interfaces and aluminum corrosion. However, except the Li/SPE/NCA batteries running up to 4.45 V, during the subsequent cycles these processes were increasingly diminished, whereas the remaining but steadily decreasing capacity fading was assumed to arise mainly from irreversible structural changes in the cathode material, remaining aluminum corrosion, deformation and loss of electric contact at the cathode/Al^0 interface. In addition, it was suggested, that the presence of Pyr$_{14}$TFSI ionic liquid in the composite cathode not only decreased the interfacial resistance but presumably also diminished the dissolution of aluminum corrosion products into the polymer electrolyte. In contrast, remarkable continuous decomposition of the polymer electrolyte in presence of the 4 V-class composite cathode could not be proved, most likely due to the formation of a surface film at the cathode/polymer electrolyte interface, thus inhibiting further reaction.

Acknowledgments

References

[1] B. Scrosati, J. Garche, J. Power Sources 195 (2010) 2419.
[2] Y. Xia, T. Fujieda, K. Tatsumi, P.P. Prosini, T. Sakai, J. Power Sources 92 (2001) 234.
[3] J.H. Shin, W. Henderson, S. Passerini, Electrochem. Commun. 5 (2003) 1016.
[4] A. Hooper, J.M. North, Solid State Ionics 9 (1983) 1161.
[5] D. Linden, Handbook of Batteries and Fuel Cells, McGraw Hill, New York, USA, 1984.
[6] M. Armand, J.M. Chabagno, M. Duclot, Fast Ion Transport in Solids, Elsevier, New York, USA, 1979.
[7] J.H. Shin, W. Henderson, G.B. Appetecchi, F. Alessandrini, S. Passerini, Electrochim. Acta 50 (2005) 3859.
[8] J.H. Shin, W.A. Henderson, C. Tizzani, S. Passerini, S.S. Jeong, K.W. Kim, J. Electrochem. Soc. 153 (2006) A1649.
[9] G.T. Kim, G.B. Appetecchi, F. Alessandrini, S. Passerini, J. Power Sources 171 (2007) 861.
[10] G.B. Appetecchi, M. Carewska, F. Alessandrini, P.P. Prosini, S. Passerini, J. Electrochem. Soc. 147 (2000) 451.
[11] S. Matsui, T. Muranaga, H. Higobashi, S. Inoue, T. Sakai, J. Power Sources 97 (2001) 772.
[12] G.B. Appetecchi, J. Hassoun, B. Scrosati, F. Croce, F. Cassel, M. Salomon, J. Power Sources 124 (2003) 246.
[13] P. Prosini, T. Fujieda, S. Passerini, Electrochem. Commun. (2000).
[14] Y. Kobayashi, H. Miyashiro, H. Takeuchi, H. Shigemura, N. Balakrishnan, M. Tabuchi, H. Kageyama, T. Iwahori, Solid State Ionics 152 (2002) 137.
[15] S. Seki, Y. Kobayashi, H. Miyashiro, Y. Mita, T. Iwahori, Chem. Mater. 17 (2005) 2041.
[16] S. Seki, Y. Kobayashi, H. Miyashiro, A. Usami, Y. Mita, N. Terada, J. Electrochem. Soc. 153 (2006) A1073.
[17] Q. Li, N. Imanishi, A. Hirano, Y. Takeda, O. Yamamoto, J. Power Sources 110 (2002) 38.
[18] Y. Takeda, N. Imanishi, O. Yamamoto, Electrochemistry 77 (2009) 784.
[19] Y. Matoba, S. Matsui, M. Tabuchi, T. Sakai, J. Power Sources 137 (2004) 284.
[20] G.T. Kim, G.B. Appetecchi, M. Carewska, M. Joost, A. Balducci, M. Winter, S. Passerini, J. Power Sources 195 (2010) 6130.
[21] M. Wetjen, G.T. Kim, M. Joost, M. Winter, S. Passerini, Electrochim. Acta 87 (2013) 779.
[22] J.H. Shin, W.A. Henderson, S. Passerini, J. Electrochem. Soc. 152 (2005) A978.
[23] J.H. Shin, W.A. Henderson, S. Passerini, Electrochem. Solid-State Lett. 8 (2005) A125.
[24] J.H. Shin, W.A. Henderson, S. Scaccia, P.P. Prosini, S. Passerini, J. Power Sources 156 (2006) 560.
[25] D. MacFarlane, J. Huang, M. Forsyth, Nature 402 (1999) 792.
[26] D. MacFarlane, P. Meakin, J. Sun, N. Amini, M. Forsyth, J. Phys. Chem. B 103 (1999) 4164.
[27] P.C. Howlett, N. Brack, A.F. Hollenkamp, M. Forsyth, D.R. MacFarlane, J. Electrochem. Soc. 153 (2006) A595.
[28] J. Xiao, N.A. Chernova, M.S. Whittingham, Chem. Mater. 22 (2010) 1180.
[29] S.B. Majumder, S. Nieto, R.S. Katiyar, J. Power Sources 154 (2006) 262.
[30] G.B. Appetecchi, M. Montanino, D. Zane, M. Carewska, F. Alessandrini, S. Passerini, Electrochim. Acta 54 (2009) 1325.
[31] G.B. Appetecchi, S. Scaccia, C. Tizzani, F. Alessandrini, S. Passerini, J. Electrochem. Soc. 153 (2006) A1685.
[32] B. Rupp, M. Schmuck, A. Balducci, M. Winter, W. Kern, Eur. Polym. J. 44 (2008) 2986.
[33] M. Joost, M. Kunze, S. Jeong, M. Schönhoff, M. Winter, S. Passerini, Electrochim. Acta 86 (2012) 330.
[34] M. Joost, Solid Polymer Electrolytes, University of Muenster, 2012.
[35] I. Belharouak, W. Lu, D. Vissers, K. Amine, Electrochem. Commun. 8 (2006) 329.
[36] B. Scrosati, F. Croce, G.B. Appetecchi, L. Persi, Nature 394 (1998) 456.
[37] J. Xi, X. Qiu, X. Ma, M. Cui, J. Yang, X. Tang, W. Zhu, L. Chen, Solid State Ionics 176 (2005) 1249.
[38] W. Gorecki, M. Jeannin, E. Belorizky, C. Roux, M. Armand, J. Phys. Condensed Matter 7 (1995) 6823.
[39] G.B. Appetecchi, G.T. Kim, M. Montanino, F. Alessandrini, S. Passerini, J. Power Sources 196 (2011) 6703.
[40] J. MacDonald, Impedance Spectroscopy, John Wiley & Sons, New York, USA, 1987.
[41] B. Boukamp, Solid State Ionics 18–19 (1986) 136.
[42] B. Boukamp, Solid State Ionics 20 (1986) 31.
[43] S.-T. Myung, Y. Hitoshi, Y.-K. Sun, J. Mater. Chem. 21 (2011) 9891.
[44] Q. Li, N. Imanishi, Y. Takeda, A. Hirano, O. Yamamoto, Ionics 8 (2002) 79.
[45] Y. Chen, J. Electrochem. Soc. 146 (1999) 1310.
[46] Q. Li, T. Itoh, N. Imanishi, A. Hirano, Y. Takeda, O. Yamamoto, Solid State Ionics 159 (2003) 97.
[47] G.B. Appetecchi, G.T. Kim, M. Montanina, M. Carewska, R. Marcilla, D. Mecerreyes, I. De Meatza, J. Power Sources 195 (2010) 3668.
[48] J.R. MacDonald, Solid State Ionics 13 (1984) 147.
[49] P. Jasinski, V. Petrovsky, T. Suzuki, H.U. Anderson, J. Electrochem. Soc. 152 (2005) J27.
[50] V. Etacheri, R. Marom, R. Elazari, G. Salitra, D. Aurbach, Energy Environ. Sci. 4 (2011) 3243.
[51] Y. Xia, K. Tatsumi, T. Fujieda, P.P. Prosini, T. Sakai, J. Electrochem. Soc. 147 (2000) 2050.
[52] H. Yang, K. Kwon, T.M. Devine, J.W. Evans, J. Electrochem. Soc. 147 (2000) 4399.
[53] B. Garcia, M. Armand, J. Power Sources 132 (2004) 206.
[54] R.-S. Kühnel, N. Böckenfeld, S. Passerini, M. Winter, A. Balducci, Electrochim. Acta 56 (2011) 4092.
[55] R.-S. Kühnel, M. Lübke, M. Winter, S. Passerini, A. Balducci, J. Power Sources 214 (2012) 178.